Low-loss rib waveguides containing Si nanocrystals embedded in SiO_2

P. Pellegrino,[a] B. Garrido, C. Garcia, J. Arbiol, and J. R. Morante
Electronic Materials and Engineering (EME), Department d'Electrònica, Universitat de Barcelona, Martí i Franqués, 1, 08028 Barcelona, Spain

M. Melchiorri, N. Daldosso, and L. Pavesi
Department of Physics, University of Trento, Via Sommarive 14, I-38050 Povo (Trento), Italy

E. Scheid and G. Sarrabayrouse
Laboratoire d'Analyse et d'Architecture des Systèmes (LAAS)-Centre National de la Recherche Scientifique (CNRS), 7, Avenue du Colonel Roche, 31077 Toulouse, France

(Received 1 June 2004; accepted 1 February 2005; published online 25 March 2005)

We report on the study and modeling of the structural and optical properties of rib-loaded waveguides working in the 600–900-nm spectral range. A Si nanocrystal (Si-nc) rich SiO_2 layer with nominal Si excess ranging from 10% to 20% was produced by quadrupole ion implantation of Si into thermal SiO_2 formed on a silicon substrate. Si-ncs were precipitated by annealing at 1100 °C, forming a 0.4-μm-thick core layer in the waveguide. The Si content, the Si-nc density and size, the Si-nc emission, and the active layer effective refractive index were determined by dedicated experiments using x-ray photoelectron spectroscopy, Raman spectroscopy, energy-filtered transmission electron microscopy, photoluminescence and *m*-lines spectroscopy. Rib-loaded waveguides were fabricated by photolithographic and reactive ion etching processes, with patterned rib widths ranging from 1 to 8 μm. Light propagation in the waveguide was observed and losses of 11 dB/cm at 633 and 780 nm were measured, modeled and interpreted. © *2005 American Institute of Physics*. [DOI: 10.1063/1.1876574]

I. INTRODUCTION

Si-based photonics has already demonstrated most of the photonic components within Si technology, such as low-loss waveguides [oxides, nitrides, oxinitrides, SiGe, and Silicon-on-insulator (SOI)], optical modulators (Si thermo-optic modulators and SiGe–Si Mach–Zender), and switches and detectors [avalanche photodiodes (APD) from SiGe and Ge *p-i-n* photodiodes].[1] One of the major open issues is the achievement of an efficient and reliable light source. A further step ahead is to find a low-loss optically active medium that can be used for achieving optical gain and then pave the way to a Si-based laser. Silicon nanocrystal (Si-nc) rich waveguide could be such a medium.

The luminescent properties of Si-nc have been studied for more than a decade.[2–6] They show a certain number of striking properties, which look like a direct consequence of quantum confinement of generated excitons. Si-nc present tunable photo- and electroluminescence in the visible–near-infrared range and recently, relatively efficient light-emitting devices (LEDs) have been demonstrated.[7,8] The observation of optical gain in Si nanostructures provides a breakthrough towards the realization of a coherent Si-based light source.[9,10] To take advantage of these effects, low-loss waveguides should be fabricated from such active material in order to produce edge-emitting structures. At the same time, the discovery of an efficient sensitizing action of Er provided by Si-nc pushed the research towards Er-based optical waveguide amplifiers,[11,12] allowing for the use of broadband pumping sources.[13–15] Low-loss silica-based waveguides doped both with Si-nc and Er and working in the near infrared are needed for these purposes. In this context, investigations of light propagation in heterogeneous glass materials containing Si-nc are required, since the control and reduction of optical losses is a primary requirement to achieve net optical gain. Few loss studies have been recently reported only on slab waveguides with Si-nc.[16–18]

In this work first we present a thorough study on the physical and optical characteristics of rib-loaded waveguides containing Si-nc obtained by ion implantation of Si into silica to create a well-controlled Si excess profile followed by an annealing step for the precipitation and growth of the Si nanoclusters. The structural and optical characteristics of the active material have been studied, leading to a good knowledge and control of its properties. X-ray photoelectron spectroscopy (XPS), Raman spectroscopy, energy-filtered transmission electron microscopy (EFTEM), and photoluminescence (PL) have allowed determining the shape of the implanted profile, the actual Si excess introduced, the crystalline fraction of the Si excess phase, the grain-size distribution, and the emission properties of the nanoparticles. Then, rib-loaded waveguides were fabricated by photolithography and reactive ion etching. An accurate characterization of the optical losses in the visible range was then performed by surface light-scattering experiments and insertion losses measurement at 630 and 780 nm. A model is proposed which accounts for the measured 11-dB/cm loss values.

II. EXPERIMENTAL DETAILS

In order to introduce Si excess inside the oxide matrix, multiple Si^+-ion implantations have been performed in both

[a]Electronic mail: paolo@el.ub.es

2-μm-thick SiO_2 films, thermally grown on Si and pure fused quartz wafers. Ion energies, ranging from 35 to 200 keV, and relative doses of the multiple implantations were chosen to give rise to a "box-like" Si supersaturation up to a depth of about 0.4 μm. This yields planar waveguides with constant Si content in depth. The total ion doses were tailored to introduce a Si excess ranging from 10% to 20% of the atomic concentration in SiO_2 before implantation. Afterwards the samples were annealed at 1100 °C in N_2 atmosphere for different times, from 1 min up to 16 h.

Optical-absorption measurements of the processed fused silica wafers have been performed in the visible and ultraviolet range (900–190 nm) by means of an UV-2101 Shimadzu spectrophotometer. Raman-scattering measurements on the same set of samples were made by exciting with a 514-nm Ar laser line and detecting the signal by a microobjective (NA=0.95) and a cooled charge-coupled device (CCD) array detector. Secondary-ion-mass spectroscopy (SIMS) measurements were carried out by means of an A-DIDA 3000-30 Atomica microanalyzer using an Ar^+ primary ion beam with a net impact energy of 12 keV. The beam current was typically 0.4 μA and the Ar^+ ions were rastered over a surface area of 500×500 μm^2. Positive secondary ions were collected from the central part of this area (around 200 μm in diameter).

Conventional transmission electron microscopy (TEM) in dark field was used to image the different multilayer structure using a Philips 200-kV microscope equipped with a Gatan 666 spectrometer. EFTEM was employed to monitor the size distribution of nanocrystals and its evolution with the implanted dose. The observations were performed by means of a field-emission 200-kV Jeol 2010F equipped with a Gatan image filter (GIF 2000) which adds energy-loss spectroscopy and filtered imaging capabilities. In order to enhance the nanocrystals contrast on the TEM image, we energetically filter the electron energy-loss spectroscopy (EELS) spectra, by using the GIF, around the Si plasmon (placed at 17 eV), which is sufficiently separated from the SiO_2 plasmon (placed at 26 eV).

We have performed systematic luminescence measurements in all samples by using a 60-mW He–Cd laser for ultraviolet excitation at 325 nm. The luminescent emission was analyzed in backscattering mode by a monochromator and detected with a GaAs Hamamatsu photomultiplier. The standard chopper–lock-in technique was used to increase the signal-to-noise ratio. All the measurements were corrected for the system response measured with a calibrated tungsten lamp.

The waveguides have been characterized by coupling-in visible light from laser diodes (633 nm—few milliwatt, 780 nm—about 7 mW) through a tapered fiber mounted on a nanopositioning system (Melles–Griott nanomax-TS). A top-view observation of scattered light has been performed by means of an optical microscope and a CCD camera mounted on top of the measuring system. A front-view observation of the exit facet of the waveguide has been obtained by using a microscope objective ($40\times$) matched to a zoom (Navitar $12\times$) mounted on a high-performance CCD camera (Dalstar SMD-1M15) computer controlled by the LBA-500 SPIRICON beam analyzer software. A prism beam splitter allows to split the transmitted light in two parts: one is directed to the CCD camera, the other is directed to a calibrated photodiode, which yields power measurement of the waveguide transmitted light.

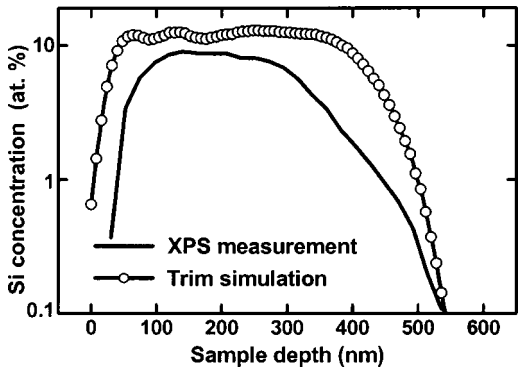

FIG. 1. Si-implanted profile, as obtained by transport of ions in matter (TRIM) simulation and XPS analysis.

III. CHARACTERIZATION OF THE ACTIVE MATERIAL

A. XPS measurements

The Si-implanted profile was obtained by the XPS analysis and compared with simulation by SRIM2000 (Fig. 1). The simulated profile was used to calibrate the energies and doses of the implantation. Some significant differences are observed between simulation and measurements: (1) the central flat profile region is 300 nm wide in measurements while it was expected to be 400 nm according to calculations; (2) the measured profile shows broader tails (mainly beyond 350 nm) than the calculated one. This could affect modal confinement in the waveguides. It is worth noticing that no variation in the excess silicon profile shape was observed by increasing the implantation dose. Confirmation of the XPS profile comes from the SIMS measurement (Fig. 2).

Let us evaluate the Si excess content in the implanted region. The XPS measurements allow to determine the stoichiometric ratio $x=[O]/[Si]$, where $[O]$ and $[Si]$ are the total atomic concentrations of oxygen and silicon in the layer. From x and the stoichiometric formula SiO_2, it is easy to calculate the excess silicon content $[Si]_{excess}=(1-x/2)/(1$

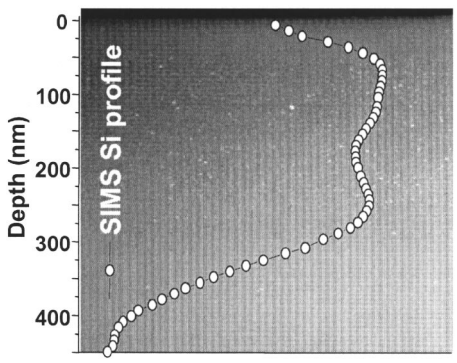

FIG. 2. Si profile of the 9.5% sample as measured by SIMS superimposed to the TEM image of the corresponding region.

TABLE I. Implanted Si excess and corresponding nanocrystal density and size.

	Si excess in the implanted layer (at. %)				Si nanocrystals size		
Sample code	Simulated (with respect to the unimplanted target)	Simulated (with respect to the implanted target)	Simulated (including swelling)	Determined by XPS	Mean value (nm)	Dispersion (nm)	Density of Si nanocrystals ($\times 10^{18}$ cm^{-3})
A	20	16.7	13	13	4.6	0.6	4
B	15	13	10	9.5	4.1	0.5	4
C	10	9	7	7	3.6	0.4	4

$+x$) [Si] (column 5 in Table I). For the three sets of samples, ion doses have been tailored to 10%, 15%, and 20% of 6.66×10^{22} cm^{-3}, the atomic concentration of SiO_2 (column 2 in Table I). They correspond to 9%, 13%, and 16.7% Si excess, respectively, if it is referred to the total atomic concentrations of oxygen and silicon once the layer has been implanted (column 3 in Table I). Thus these figures can be directly compared with the experimental results, and a slight difference among the two sets of values can be observed in Table I. The agreement is improved once considering swelling in the simulation (column 4 in Table I). Swelling appears when implanting to high doses. In these conditions, a plastic deformation of the oxide takes place to restore an almost constant density of SiO_x (independent of x) at equilibrium.[19,20] The relative increase in volume is directly proportional to the introduced Si excess, with a proportionality factor equal to $M_{Si}/(1/3M_{Si}+2/3M_O)$, where M_{Si} and M_O are the atomic masses of Si and O, respectively.

B. Raman and absorption measurements

Additional information about the microstructure of the layers has been obtained by means of Raman and visible absorption measurements on Si-nc samples prepared on transparent substrate (fused silica glasses). Representative Raman spectra as a function of the annealing treatments are shown in Fig. 3 for the highest Si excess sample. A careful analysis of the Raman spectra involved the subtraction of the contribution coming from the silica substrate. In the as-implanted samples (zero annealing time in Fig. 3), the Raman spectrum is dominated by a broad (70-cm^{-1} bandwidth) structure peaking at 480 cm^{-1}, which is a typical signature of the transverse-optical mode of amorphous Si. It is quite surprising to find signal due to amorphous Si in the as-implanted samples. This suggests that most of the implanted silicon is already in small amorphous clusters even in the as-implanted state. The high local temperatures reached during the implantation and the enhanced diffusivity of Si and O due to radiation damage would favor such a situation. After annealing at 1100 °C for 20 min, the Raman spectrum shows a narrow asymmetric peak centred around 521 cm^{-1}, indicating the phase separation and rapid crystallization of the amorphous Si clusters. Further annealing at the same temperature (for durations up to 8 h) does not appreciably modify neither the shape nor the intensity of the Si-nc signal. This is in agreement with a previously published study by Garrido *et al.*,[21] in which it is shown that the asymptotic Ostwald ripening growth stage of the population of Si-nc is reached after few minutes of annealing at 1100 °C. Furthermore, the integrated Raman signal due to Si-nc increases with the implanted dose and this strongly supports the conclusion that the overall excess Si has precipitated into the Si-nc (see Fig. 4); additional infrared experiments corroborated that the matrix is stoichiometric SiO_2.

Optical transmission measurements (Fig. 5) show that (1) the energy onset of absorption increases as the Si excess content in the sample decreases, (2) the line shape of the absorption spectra is very similar for all the samples, once

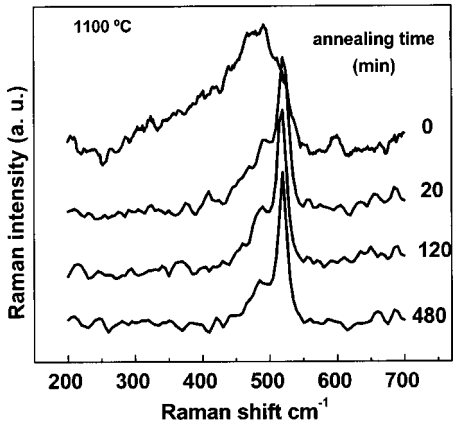

FIG. 3. Raman spectra of the sample with 13% Si excess, annealed at 1100 °C for the different times reported in the graph. The spectra have been vertically displaced for the sake of clarity.

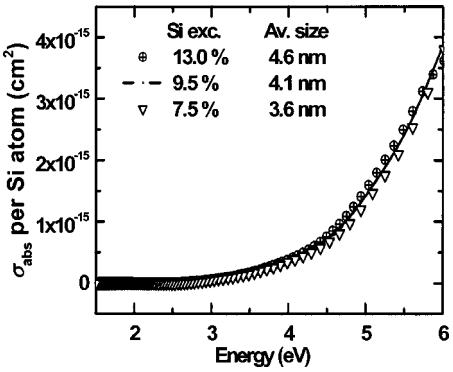

FIG. 4. Optical-absorption cross section per Si atom for the three Si concentrations.

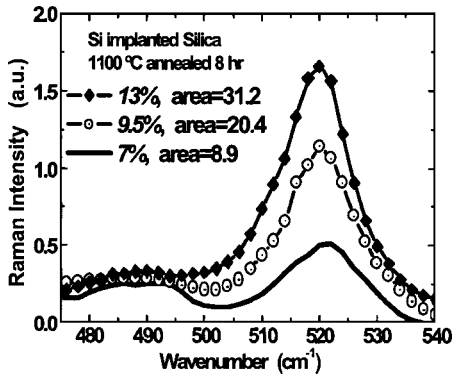

FIG. 5. Raman spectra of the 8-h annealed samples for the three Si concentrations.

rescaled to the implanted dose, and (3) after the first 20 -min annealing the absorption spectrum does not change.

C. Transmission electron microscopy measurements

In Fig. 2 a typical TEM image is shown in dark field and displays a uniform region with a high density of Si-nc which lies at about 50 nm from the surface and extends up to around 300 nm in depth, right in correspondence to the flat portion of the Si implantation as obtained from the SIMS signal which has been superimposed in the same figure. Just small variations in the thickness of the nanocrystal-rich layer have been observed in the wafers implanted to different doses. By varying the implanted dose a tuning in the average size and density of Si-nc is expected. The EFTEM analysis provides valuable information to this regard, allowing to buildup a statistical histogram of the nanocrystal size as a function of the Si excess.

A typical EFTEM image is given in Fig. 6 for the sample with 9.5% of the Si excess. Repeated measurements for each Si excess allow to prepare a statistical histogram of the nanoparticle size, as reported in Fig. 7 for the various Si excess. A systematic increase of the average size of the Si-nc with the Si excess is observed, together with a rather small dispersion around the mean value (0.3–0.5 nm typical). The typical sizes range from 3.6 nm (7% Si excess) to 4.1 nm (9.5% Si excess) and up to 4.6 nm (13% Si excess). It is worth noticing that high-resolution TEM (HRTEM) image analysis yields lower values for the Si-nc size; values between 2.5 and 3 nm were obtained.

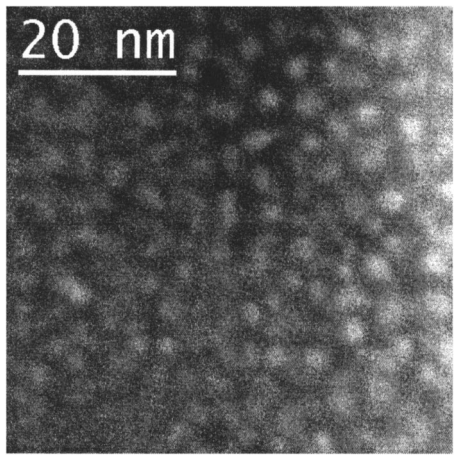

FIG. 6. EFTEM image of the implanted region of the 9.5% sample.

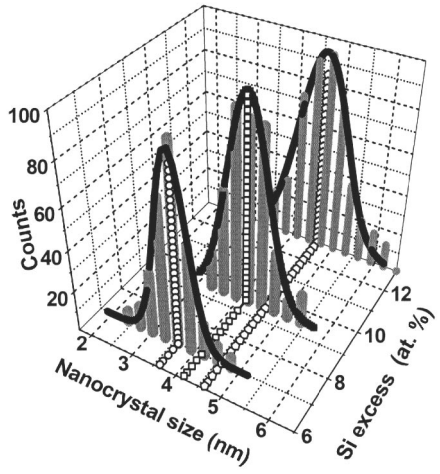

FIG. 7. Statistical histograms of the nanocrystal size distributions as a function of the Si content, as obtained from the EFTEM measurements.

By assuming a perfect phase separation between the excess Si and SiO_2 and by combining the values of both the Si excess and average particle size, an estimation of the density of Si-nc can be performed. We obtain a density of $\sim 4 \times 10^{18}$ Si-nc/cm^3, independent on the Si excess value. The observation by the EFTEM imaging that the areal density of the nanoparticles is quite similar in all kinds of samples provides an additional support to this evaluation.

D. Luminescence measurements

Typical PL spectra are presented in Fig. 8, with an inset showing the dependence of the integrated PL intensity with the Si excess. The luminescence spectrum is dominated by a strong band due to Si-nc recombination at 800 nm and a weak defect-related emission at 400 nm. Two results are very clear from the data, the PL redshifts and the PL intensity increase with increasing the Si excess. The redshift of the maximum is consistent with the increase in the Si-nc size measured by EFTEM, while the peak spectral positions are in agreement with previous results from single Si^+-ion implants in thermal oxides.[21] The increase in the PL intensity

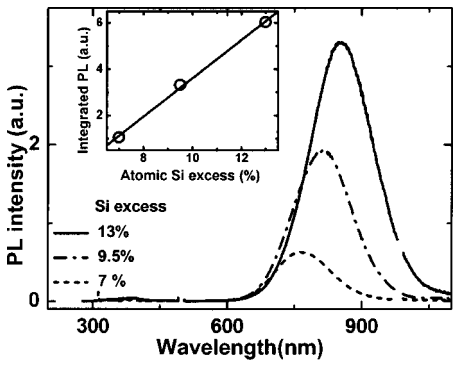

FIG. 8. PL spectra measured for the three Si concentrations. The inset shows the integrated photoluminescence as a function of the Si excess.

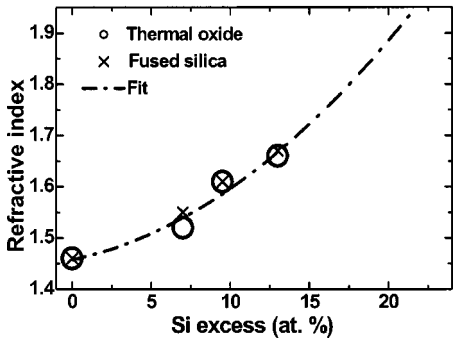

FIG. 9. Refractive index of the active layer as a function of the introduced Si excess. The values obtained by *m*-lines measurements at 632.8 nm have been interpolated by a polynomial fit.

follows the variation of the absorption cross section σ with the implanted dose (see Fig. 5, where σ has been normalized to the implanted dose); it appears that the density of states available for excitation at high energies (the blue-UV range) is proportional to the number of the introduced Si atoms and not to the density of Si nanocrystals.

E. Refractive index measurements

m-lines measurement yields the refractive index and the effective thickness of the core layer in the waveguide structure. We found a thickness of 340 nm, a value independent of the Si excess content. On the contrary, the refractive index values depend on the Si excess. Figure 9 reports the measured values together with those for fused silica (substrate) and the unimplanted thermal oxide. As expected within a simple effective-index model, the refractive index increases with the Si excess. Such dependence of the refractive index with the silicon excess has been corroborated by ellipsometry measurements (results not shown). The values obtained here for the refractive index at 632 nm are about 7% higher than those obtained by Charvet *et al.* for similar Si excess in sputtered samples.[22] This difference can be accounted for by the higher compactness of our samples.

In summary, the overall characterization of the active layers allowed to determine important parameters for the interpretation of the losses in the waveguide structures. Moreover, it has been possible to establish some new original results regarding ion-beam synthesis of Si-ncs in SiO_2, as summarized in the following. At the processed temperature, the whole implanted Si has been precipitated in the form of Si nanocrystals, with an average size ranging from 3.6 to 4.6 nm, depending on the ion dose. These values are systematically larger than the ones found in many early reports on the formation of Si-ncs by ion-beam synthesis,[3–5] where the conventional TEM analysis was carried out. Such a technique has been revealed to underestimate the Si grain size, as pointed out in Ref. 6 for the Si-nc rich SiO_2 layers grown by chemical-vapor deposition. Similar to our findings, it is interesting to note how these authors stress the importance to establish quite firmly the crystalline/amorphous ratio of the nanoprecipitated for a chosen annealing regime.

The density of Si particles has been found completely independent on the introduced excess, laying close to 4×10^{18} cm^{-3} for the chosen processing conditions. Thus, for the explored range, an increase of almost 100% in the ion dose does not imply a corresponding variation in the Si-ncs density, which stays constant, but uniquely an overall increase of the Si-ncs size. This finding may shed some light on the studies of the kinetics of formation of Si-ncs in SiO_2, an important field of research, still not fully explored.[6,21]

The absorption cross section in the 3.5–64-eV spectral region scales with the implanted ion density. At these energies, the available density of states is proportional to the number of Si atoms composing the nanoparticle. Then, the presented data allow the calculation of the absorption characteristics in the blue-UV range for an arbitrary ensemble of Si-ncs, once their dimension is known.

IV. WAVEGUIDE DESIGN AND FABRICATION

A. Design

Simulations were performed in order to determine the best combination of geometrical parameters for the design of waveguides for the visible–near-infrared range (at 633 and 780 nm). Design has been done by using a photonics computer-aided design (CAD) tool for the simulation, the mode-solver software FIMMWAVE 3.0 (Photon Design Inc.), which is a fully vectorial mode finder for waveguide structures. All the simulations have been made for a signal wavelength of 780 nm. As the waveguides were to be made on the 9.5% Si excess sample, already discussed above, the active layer was taken to be 340 nm thick, with a refractive index of 1.61, as deduced by the *m*-line measurements. A refractive index of 1.45 and a thickness of 1.6 μm have been used for the SiO_2 layers and for the bottom cladding.

Two-dimensional (2D) waveguide structures are preferred with respect to one-dimensional (1D) slab waveguide, when new optical devices have to be tested. With this respect, it is important to verify that the processing to form 2D waveguides does not degrade the optical quality of the waveguide and, most important, does not introduce further losses, such as those due to sidewall scattering. A rib-loaded geometry was chosen due to the need for single mode behavior and large confinement factor, attainable with the resolution of the available lithography. Given the large contrast between the refractive index of the active and the SiO_2 layers, channel waveguides would have needed a channel width lower than 2 μm wide in order to be monomode. This restriction is less tight for a single mode rib-loaded waveguide. A set of rib widths from 2 to 8 μm was considered in order to study the effect of mode size on the losses behavior.

Both effective refractive index ($n_{TE}=1.52$ and $n_{TM}=1.51$ at 780 nm) and filling factors (66% and 62% for TE and TM fundamental modes at 780 nm) slightly increase with increasing the rib width. This is due to the chosen geometry which confines light underneath the rib. The waveguide becomes multimode for a rib width larger than 4 μm. Figure 10 shows the profile of the fundamental TE mode in the 4-μm-wide rib-loaded waveguide.

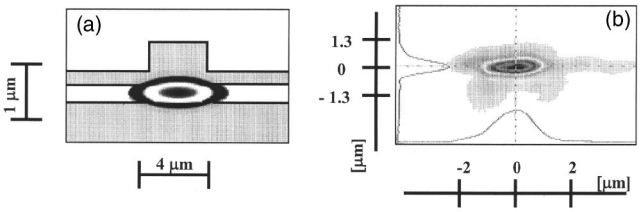

FIG. 10. Intensity plot profile of the fundamental optical mode of a 4-μm width rib loaded simulated (a) and measured by a beam analyzer (b).

B. Fabrication

A 1-μm-thick plasma-enhanced chemical-vapor deposition (PECVD) SiO_2 layer was deposited over the 4-in. wafer with the 9.5% Si excess. A 0.7-μm-thick rib structure was then formed by using standard photolithography and reactive ion etching. The mask used in the photolithographic process was patterned with 1-cm^2 squares, each containing eight groups of 2–8-μm-wide waveguides, 240 μm apart to assure proper mode isolation. The squares were subsequently cut by a dicing saw to a length of 0.95 cm. In Fig. 11 the resulting structure of staking layers is illustrated.

To test the process results, room-temperature air atomic force microscopy (AFM) images were performed by using an NT-MDT microscope. From cross-section image analysis, the mean rib height was 670 ± 50 nm and rib widths were 2.45, 4.45, 6.6, and 8.4 ± 0.05 μm for the nominal 2, 4, 6, and 8 μm, respectively. Some structures around the wall of the rib have been observed and they can be attributed to a nonperfect etching process. Moreover, the AFM images show that the profile is not sharp and the shape of the walls is trapezoidal for all rib widths.

V. LOSS MEASUREMENTS AND DISCUSSION

Efficient propagation of light was observed at 780 nm by top and front views for all the waveguides. Coupling in light has been easily achieved because of the good quality of the polished edges and the homogeneity of the sample, which resulted in efficient propagation of light in different parts of the sample.

Propagation losses measurements have been performed by looking at the surface scattered light intensity and by insertion loss measurements. The decrease of the scattered light intensity along the waveguide can be related to the propagation losses by simply fitting an exponential decay

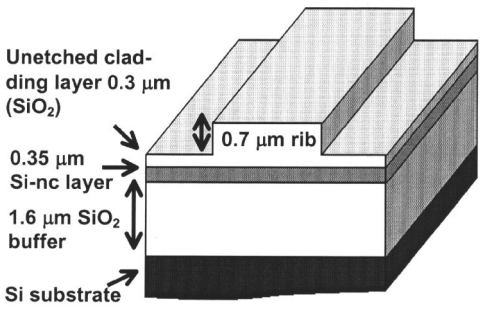

FIG. 11. Schematic picture of a channel waveguide showing the stack of the different layers with their composition and typical dimensions.

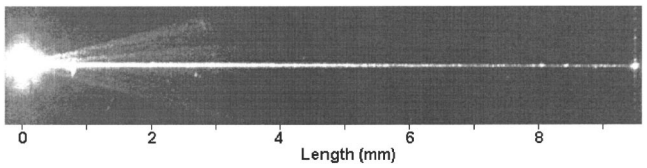

FIG. 12. Top-view image of the light scattered along the waveguide for an 8-μm-wide rib.

dependence, independently on the evaluation of coupling losses. For a discussion and validation of the method see Ref. 23. Figure 12 shows a top view of the scattered light from an 8-μm-wide rib and 0.95-cm-long waveguide. One can appreciate the good lateral confinement of the mode that propagates in the waveguide. Figure 13 shows the scattered light intensity versus waveguide length, as obtained by the image analysis, and the typical quality of the exponential decay fit to extract propagation losses at 780 nm. The contribution of the scattered light of the first 1–2 mm from the input facet is not considered in the data analysis in order to improve the signal-to-noise ratio. Averaging of multiple measurements on several waveguides with the same width was done. The propagation loss coefficients for the different rib widths are reported in Table II for two light wavelengths, 633 and 780 nm.

The insertion losses technique is based on the measurement of the power transmitted from the waveguide output facet as a function of input signal power. This technique can be useful in order to estimate the propagation losses through the waveguide, once coupling losses have been estimated. The losses through the optical collection system have been determined by measuring the transmitted power of the tapered fiber in front of the collecting microscope objective; a value of 5 dB was found. The coupling losses are due to several effects. Not perfect coupling between tapered fiber and input facet accounts for about 3 dB (20-μm separation errors) plus 2 dB (1 μm or 1 deg of misalignment errors). By considering a Gaussian input laser beam, the difference between the tapered fiber's spot size (about 5 μm) and waveguide dimensions (350 nm thick and width ranging from 2.4 to 8.4 μm) accounts for about 12 dB for the core thickness and 1–5 dB for rib width ranging from 6 to 2.4 μm. No losses due to the different numerical aperture (NA) are present because the NA of the waveguide is larger than that

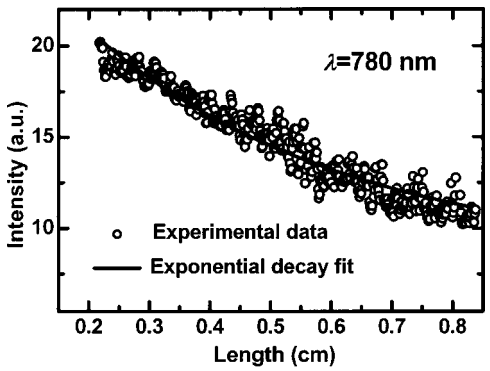

FIG. 13. Scattered light intensity at 780 nm along the waveguide for an 8 -μm-wide rib.

TABLE II. Rib widths and propagation losses.

Rib width (μm)		Propagation loss coefficient (dB/cm) as obtained by light scattering		Propagation loss coefficient (dB/cm) as obtained by insertion losses	
Nominal	Measured	780 nm	633 nm	780 nm	633 nm
8	8.4±0.05	11±1	11±0.5	~11	~13
6	6.6±0.05	12±1	12±0.5	~12	~13
4	4.45±0.05	12±1	12±0.5	~15	~13
2	2.45±0.05	21±1	19±1	~21	~19

of the input fiber. Therefore, a conservative estimate of the coupling losses is about 17 dB for the largest rib waveguide (8.4 μm), which increases up to 23 dB for the smallest (2.4 μm) waveguide measured. An experimental estimate of about 15 dB has been obtained by comparison with similar samples for which it was possible to determine the propagation losses by the cut-back technique and, hence, to deduce the coupling losses.[23]

Propagation losses coefficients have been obtained by subtracting coupling from insertion losses and are reported in Table II for light at 633 and 780 nm. It is worth noting that the two independent techniques give the same (within the error bar) loss coefficients, thus demonstrating the reliability of both experimental procedures. Furthermore, no significant differences in the propagation loss coefficient have been found by changing the wavelength of the input light from 633 to 780 nm. This is expected since no significant difference in modal confinement was observed in the waveguide simulations. We also tried coupling in light at wavelengths of 1310 and 1500 nm but no guided modes were observed, in accordance with the simulations, where no confined mode was observed at 1310 nm or longer wavelengths.

A summary of the loss data is reported in Fig. 14. It is worth noticing that the loss coefficient is mainly constant (about 11 dB/cm) for rib widths down to 4 μm, while for a value of 2.4 μm an increase up to about 20 dB/cm is observed. This can be explained mainly by considering that for small widths the rib sidewall scattering increases and the modal confinement becomes poorer. By the loss difference between large and small waveguides we estimated this contribution to be about 8 dB/cm.

Let us discuss the value of 11-dB/cm propagation losses we found for large waveguides. This value of 11 dB/cm

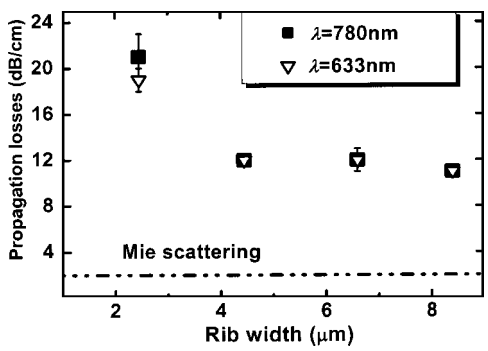

FIG. 14. Variation of the propagation losses with rib width at 633 and 780 nm.

(about 2.5 cm^{-1}) of propagation losses is quite good considering the mode confinement. No direct comparison with similar measurements on 2D waveguides is possible, as most of the results reported in the literature refer to planar (1D) waveguides. Due to a renewed interest in this kind of waveguides for optical amplification experiments, in the literature several measurements of losses have been recently reported based on the so-called shift-excitation-spot (SES) technique, the detection of the attenuation of the spontaneous emission as a function of the distance from the recording point. Optical losses of 15–20 cm^{-1} have been reported in porous silicon grains embedded in sol-gel derived SiO_2 matrix,[24] while values of 30–40 cm^{-1} have been reported for Si-nc.[25,26] Lower values (about 2.6 cm^{-1}) have been reported for thick slab waveguides at 780 nm by means of shift-excitation-spot technique.[17] In the same paper, losses of about 0.9 cm^{-1} have been found for longer propagation wavelengths (1000 nm) where Rayleigh scattering is decreased according to the well-known $1/\lambda^4$ law. Let us note that the reliability of the SES technique to measure low-loss values is quite limited due to inherent difficulties of the technique. What is important to remark here is that the processing to fabricate 2D waveguides does not degrade the optical properties of the waveguides, since the propagation loss values found in this work compare among the best results ever reported for this kind of waveguide.

Leakage losses towards the Si substrate can be ruled out because of the thick bottom cladding layer (1.6 μm). In fact, no light at the output facet has been observed from the substrate, in accordance with the simulations which show that 1 μm is sufficient to avoid leakage losses. Scattering losses due to the composite nature of the core layer have been calculated by Mie theory and result in about 2 dB/cm at 633 nm and 1 dB/cm at 780 nm.[27] Scattering losses depend on the density and size of the Si nanocrystals. Scattering losses due to interface roughnesses are not considered because of the high quality of the core and cladding layers, already discussed in the previous sections.

Finally, if we assume that the remaining 9-dB/cm losses are absorption losses we can get an upper limit estimate to the absorption cross section for Si-nc, $\sigma_{abs}=\alpha_{WG}/N\sim 5\times 10^{-19}$ cm^2, where α_{WG} are the absorption losses and N is the density of Si-nc. This value for σ_{abs} is compatible with other reported data.[28] If for the stimulated emission cross section a value of about 1×10^{-17} cm^2 is assumed,[29] we can get an estimate of the gain coefficient in these waveguides, attainable when the system is pumped with suitable high-

energy radiation. The ultimate performances of similar, optimized waveguide amplifier under optical pumping should be extremely promising, being just 11 dB/cm the measured losses and about 160 dB/cm the estimated gain coefficient.

VI. CONCLUSIONS

We have studied the formation, loss contributions, and mechanisms in waveguides made with Si nanocrystal-rich oxides. An exhaustive characterization of the active layer has been performed in order to control the formation and emission properties of the Si-nc, and get valuable physical parameters, such as the nanocrystal density and size and refractive index. Propagation losses have been measured on the processed waveguides and related to specific contributions. Asymptotic values of around 2 dB/cm for Mie scattering and 9 dB/cm for direct absorption were evaluated. These numbers are promising for the feasibility of a high-performance optical amplifier that makes use of similar optimized structures. Indeed optical gain values in excess of 40 dB/cm have been reported extensively in Si-nc-based planar waveguides.[30]

ACKNOWLEDGMENT

This work was supported by SINERGIA (European contract, Contract No. IST-2000-29650) and PROFILL projects. The authors kindly acknowledge Dr. Caroline Bonafos of the CEMES/CNRS, Toulouse for her TEM analysis and valuable discussions, the skilful assistance of people in the processing facilities at LAAS for their help in fabricating the samples, Dr. F. Sbrana for AFM analysis, F. Riboli for waveguide simulations, and D. Navarro for *m*-line measurements.

[1] *Silicon Photonics*, edited by L. Pavesi and D. Lockwood (Springer, Berlin, 2004).
[2] S. Ossicini, L. Pavesi, and F. Priolo, *Light Emitting Silicon for Microphotonics* (Springer, Berlin, 2003).
[3] T. Shimizu-Iwayama, N. Kurumado, D. E. Hole, and P. D. Townsend, J. Appl. Phys. **83**, 6018 (1998).
[4] S. Guha, J. Appl. Phys. **84**, 5210 (1998).
[5] S. Guha, S. B. Qadri, R. G. Musket, M. A. Wall, and T. Shimizu-Iwayama, J. Appl. Phys. **88**, 3954 (2000).
[6] F. Iacona, C. Bongiorno, C. Spinella, S. Boninelli, and F. Priolo, J. Appl. Phys. **95**, 3723 (2004).
[7] J. Linross and N. Lalic, Appl. Phys. Lett. **66**, 3048 (1995).
[8] J. de la Torre *et al.*, Physica E (Amsterdam) **16**, 326 (2003).
[9] L. Pavesi, L. Dal Negro, C. Mazzoleni, G. Franzò, and F. Priolo, Nature (London) **408**, 440 (2000).
[10] *Towards the First Silicon Laser*, edited by L. Pavesi, S. Gaponenko, and L. Dal Negro (Kluwer Academic Publisher, Dordrecht, 2003).
[11] G. Franzò, D. Pacifici, V. Vinciguerra, F. Priolo, and F. Iacona, Appl. Phys. Lett. **76**, 2167 (2000).
[12] K. Watanabe, M. Fuji, and S. Hayashi, J. Appl. Phys. **90**, 4761 (2001).
[13] H.-S. Han, S.-Y. Seo, and J. H. Shin, Appl. Phys. Lett. **79**, 4568 (2001).
[14] J. Lee, J. H. Shin, and N. Park, paper PDP19, OFC 2004, Los Angeles, (2004).
[15] D. Pacifici, G. Franzò, F. Priolo, F. Iacona, and L. Dal Negro, Phys. Rev. B **67**, 245301 (2003).
[16] J. Valenta, T. Ostatnicky, I. Pelant, R. G. Elliman, J. Linnros, and B. Honerlage, J. Appl. Phys. **96**, 5222 (2004).
[17] L. Khriachtchev, M. Räsänen, and S. Novikov, Appl. Phys. Lett. **83**, 3018 (2003).
[18] R. T. Neal, M. D. C. Charlton, G. J. Parker, C. E. Finlayson, M. C. Netti, and J. J. Baumberg, Appl. Phys. Lett. **83**, 4598 (2003).
[19] E. Snocks, A. Polman, and C. A. Volkert, Appl. Phys. Lett. **65**, 2487 (1994).
[20] S. Klaumünzer, L. Changlin, and G. Schumacher, Appl. Phys. Lett. **51**, 97 (1987).
[21] B. Garrido, M. López, C. García, A. Pérez-Rodríguez, J. R. Morante, C. Bonafos, M. Carrada, and A. Claverie, J. Appl. Phys. **91**, 798 (2002).
[22] S. Charvet, R. Madelon, F. Gourbilleau, and R. Rizk, J. Appl. Phys. **85**, 4032 (1999).
[23] N. Daldosso *et al.*, IEEE-Journal of Lightwave Technology 22, 1734 (2004).
[24] K. Luterová, K. Dohnalová, V. Svrcek, I. Pelant, J. P. Likforman, O. Crégut, P. Gilliot, and B. Hönerlage, Appl. Phys. Lett. **84**, 3280 (2004).
[25] J. Ruan, P. M. Fauchet, L. Dal Negro, M. Cazzanelli, and L. Pavesi, J. Appl. Phys. **83**, 5479 (2003).
[26] L. Dal Negro, M. Cazzanelli, B. Danese, L. Pavesi, F. Iacona, G. Franzò, and F. Priolo, J. Appl. Phys. **96**, 5747 (2004).
[27] H. C. van de Hulst, *Light Scattering by Small Particles* (Dover Publications, New York, 1981).
[28] L. Khriachtchev, Appl. Phys. Lett. **81**, 1357 (2002).
[29] L. Dal Negro *et al.*, Physica E (Amsterdam) **16**, 297 (2003).
[30] L. Pavesi, Mater. Today **8**, 18 (2005).